Voigt wave investigation in the KGd(WO 4) 2:Nd biaxial laser crystal

Alain Brenier

Journal of Optics 17, 075603 (2015). http://dx.doi.org/10.1088/2040-8978/17/7/075603

Voigt wave investigation in the $KGd(WO_4)_2$:Nd biaxial laser crystal

Alain Brenier
Institut Lumière Matière, UMR5306 Université Lyon 1-CNRS, Université de Lyon 69622 Villeurbanne cedex, France
alain.brenier@univ-lyon1.fr

Abstract : *We have investigated the Nd^{3+}-doped $KGd(WO_4)_2$ biaxial laser crystal for wave propagation directions in the vicinity of the optical axis at wavelengths tunable around 800 nm. The angular absorption distribution was found strongly anisotropic. Increasing absorption, the optical axis splits in two new ones able propagating unchanged a left or a right circularly polarized light and able propagating a circularly polarized Voigt wave with a linear spatial dependence. The intensities of the transmitted light in different configurations of polarizations were investigated. The angular displacement of the two optical axes versus the absorbed wavelengths was measured and explained with a single oscillator model. The light energy propagation was found distributed inside a crescent-shaped area.*
Keywords: biaxial crystals, laser crystals.

1. Introduction

The $KGd(WO_4)_2$ (KGW) and $KGY(WO_4)_2$ (KYW) crystals are very similar materials well-known for optical applications and commercially available. Belonging to the C2/c space group they are biaxial, monoclinic and centro-symmetric.

The growth, mechanical, thermo-physical, spectroscopic and third order nonlinear optical properties of these Nd-doped crystals have been extensively studied [1-3] while they are excellent laser materials [4] and efficient stimulated Raman scattering self-converter. Let us cite the generation of an eye-safe radiation at 1538 nm from the 1351 nm laser channel from the 901 cm^{-1} A_g vibrational mode [5] of the KGW:Nd. The KGW and KYW crystals doped with Yb^{3+} were favourably evaluated as laser materials [6] thanks to a small quantum defect, a high absorption near 981 nm and a high peak emission cross-section. Their broadband emission can be exploited for efficient ultra-short pulse generation [7-11]. On the other hand these materials have been proved efficient for spectral tuning, specially by inserting a volume Bragg grating inside the cavity [12, 13].

Most often the propagation direction is along a principal axis but not necessarily: other directions can have much interest. A two-frequency laser was realized with a Yb^{3+} doped $KGd(WO_4)_2$ crystal oriented in the N_m-N_g principal plane [14-15] in order to play with the relative emission cross-sections of the two modes. Athermal directions defined as zero change in optical path length as a function of temperature were found lying in the N_m-N_g plane and in the **Np**-N_g plane in Yb^{3+} doped $KGd(WO_4)_2$ crystal [16] and lasing along these directions under high pump power mitigates the thermal lens and the beam astigmatism [17]. Let us mention a few experiments which have a special interest for our present work: the wave propagation along an optical axis of a transparent biaxial crystal leads to the well-known phenomenon of internal conical refraction [18]. The flux of light energy is split into a cone and finally a ring instead of being doubly-refracted as in the other wave directions. Thanks to this property, an efficient conical refraction KGW:Nd laser was demonstrated to have an excellent beam quality [19]. A KGW:Yb laser was built with a polarization state selected in an arbitrarily direction without any additional cavity component [20]. Polarization

demultiplexing and multiplexing [21] was achieved for free-space optical communication applications. Optical trapping of micro-spheres [22] is another interesting application of optical axis wave propagation. The conical refraction of Gaussian beams in the KGW crystal was nicely studied (experimentally and theoretically) by some authors [23-27], while conical refraction of Laguerre-Gauss beams has distinct features [28]. The unique spatial polarization distribution inside the Airy disk area obtained from the conical refraction trough a thin biaxial crystal has been utilized in enhanced resolution microscopy [29]. Ring-shaped laser beams, i. e. beams with a circular intensity distribution with a dark central area, have much interesting applications. For example they can be used for efficient annular pumping of lasers generating directly Laguerre-Gauss modes [30, 31]. Let us cite also their role in the stimulated emission depletion (STED) microscopy: they depopulate fluorescent proteins in an excited state towards their ground state except in a central area with a few nanometers in size, from which the fluorescence can be detected with a not-diffracted spatial resolution [32, 33].
Elliptically polarized modes are poorly investigated in the field of lasers because most of applications are nicely covered using the linear polarized modes of the transparent crystal [34]. However in an absorbing or amplifying crystal, mainly for directions close to the optical axes, the modes which can be propagated unchanged are elliptically polarized [35-37]. Polarization properties of lasing near these directions have been investigated recently in KGW:Nd [38].
This paper is devoted to wave propagation along the optical axes of the KGW:Nd biaxial laser crystal in a spectral range of wavelengths including absorption. The absorption transition chosen is $^4I_{9/2} \rightarrow {}^4F_{5/2}$ around 800 nm due to its interest for laser diode pumping and its high strength and anisotropy. The Voigt wave phenomenon, the wavelength dependence of the optical axes angular position and the internal conical refraction are investigated.

2. Theoretical background

2.1 The Voigt wave

The electromagnetic wave properties and in particular the polarizations and spectroscopic properties (absorption and amplification coefficients in cm^{-1}) of a doped laser material are fully obtained in any direction of propagation for the two modes from the linear permittivity tensor $\underline{\underline{\varepsilon}}$, wavelength dependent and including eventually an imaginary part, through Maxwell equations and supposed at this initial step to be expressed in the **X**, **Y**, **Z** dielectric frame.
Due to the transverse behaviour of the dielectric displacement vector $\mathbf{D}$, it is convenient to work and express the permittivity tensor in a frame $\mathbf{x_1}$, $\mathbf{x_2}$, $\mathbf{x_3}$ whose third axis $\mathbf{x_3}$ is parallel to the propagation direction wave-vector $\mathbf{k}(\theta,\varphi)$ defined per the polar and azimuthal angles (θ, ϕ):

$$\underline{\underline{\varepsilon}}(\theta,\varphi) = S(\theta,\varphi)\,\underline{\underline{\varepsilon}}\,S^T(\theta,\varphi) \qquad (1)$$

where $S(\theta,\varphi)$ is the 3-D rotation making the (X, Y,Z)→(x_1, x_2, x_3) coordinate transfer (in other words the $\mathbf{x_1}$, $\mathbf{x_2}$, $\mathbf{x_3}$ cartesian frame coincides locally with the $\mathbf{e_\theta}$, $\mathbf{e_\phi}$, $\mathbf{e_r}$ unit vectors of the spherical coordinates).
Let us use the notations:

$$\delta_{11} = \underline{\underline{\varepsilon}}_{11}\underline{\underline{\varepsilon}}_{33} - \underline{\underline{\varepsilon}}_{13}\underline{\underline{\varepsilon}}_{31} \qquad \delta_{12} = \underline{\underline{\varepsilon}}_{12}\underline{\underline{\varepsilon}}_{33} - \underline{\underline{\varepsilon}}_{13}\underline{\underline{\varepsilon}}_{32}$$
$$\delta_{21} = \underline{\underline{\varepsilon}}_{21}\underline{\underline{\varepsilon}}_{33} - \underline{\underline{\varepsilon}}_{23}\underline{\underline{\varepsilon}}_{31} \qquad \delta_{22} = \underline{\underline{\varepsilon}}_{22}\underline{\underline{\varepsilon}}_{33} - \underline{\underline{\varepsilon}}_{23}\underline{\underline{\varepsilon}}_{32} \qquad (2)$$

Monochromatic propagation modes are found inserting $\mathbf{E}(x_3)\exp(ik\,x_3)$ solutions in the propagation equations [38, 39] and the result is the well-known Fresnel equation which is the characteristic equation of the 2-dimension eigen-value electro-magnetic problem. Its roots are the two wavenumbers given by the following formula :

$$k_{a,b}(\theta,\varphi) = \omega\left[\frac{\mu_0}{2\underline{\underline{\varepsilon}}_{33}}\left\{(\delta_{11}+\delta_{22}) \pm \Delta^{1/2}\right\}\right]^{1/2} \qquad (3)$$

with $\Delta = (\delta_{22}-\delta_{11})^2 + 4\delta_{12}\delta_{21}$ being the discriminant of the Fresnel equation, *a*, *b* corresponding to + and – signs respectively.

The mode determination depends on the Δ value. If $\Delta \neq 0$ the two wavenumbers are different and two different modes can propagate, this is the general case.

If $\Delta = 0$ a double root occurs in Fresnel equation ($k_a = k_b = k$) and the propagation direction is an optical axis. If both the δ_{12} and δ_{21}coefficients vanish the axis is isotropic, this is the case when the crystal is transparent at the considered wavelength and non-gyrotropic (the $\underline{\underline{\varepsilon}}$ tensor is real). Let us here restrict to the case of non-gyrotropic crystals (it is so for the centro-symmetric KGW host): we have the simplification $\delta_{12} = \delta_{21}$. If the crystal is absorbing (or amplifying) at the considered wavelength, then δ_{12} is nonzero in the orthorhombic, monoclinic and triclinic symmetries (and zero for higher symmetries) and a new and singular propagation component appears including a linear spatial dependence: $x_3 e^{ikx_3}\begin{bmatrix}1\\ \frac{\delta_{22}-\delta_{11}}{2\delta_{12}}\end{bmatrix}$. Let us call Voigt wave this component. The propagation optical axis is singular and from the splitting in two parts of the equation $\Delta = 0$ we obtain its (θ,φ) angular orientation solving the following equation:

$$\frac{\delta_{22}(\theta,\varphi)-\delta_{11}(\theta,\varphi)}{2\delta_{12}(\theta,\varphi)} = \pm i \qquad (4)$$

The wave after a path L can be made explicit [30] with the following formula:

$$\begin{bmatrix}E_1(L)\\ E_2(L)\end{bmatrix} = \left\{\begin{bmatrix}E_1(0)\\ E_2(0)\end{bmatrix} + ikL\frac{\delta_{12}}{\delta_{11}+\delta_{22}}\begin{vmatrix}1 & E_1(0)\\ \pm i & E_2(0)\end{vmatrix}\begin{bmatrix}1\\ \pm i\end{bmatrix}\right\}e^{ikL} \qquad (5)$$

where $|\ \ |$ is the determinant of the two included vector columns, or equivalently with the following Jones matrix (to be right-multiplied by the initial wave $\begin{bmatrix}E_1(0)\\ E_2(0)\end{bmatrix}$):

$$\left\{\begin{bmatrix}1 & 0\\ 0 & 1\end{bmatrix} + ikL\frac{\delta_{12}}{\delta_{11}+\delta_{22}}\begin{bmatrix}\mp i & 1\\ 1 & \pm i\end{bmatrix}\right\}e^{ikL} \qquad (6)$$

The first term is an isotropic wave propagation (this component is propagated unchanged) and the second term (Voigt wave component) quantifies the anisotropy of the optical axis and exhibits the role of the δ_{12} coefficient.

It is straightforward from Eq. (4) and (5) that that two different kinds of optical singular axis exist: sign + leads to an axis along which a left-circular polarized wave can be propagated unchanged (except of course an exponential attenuation) and denoted “left-circular axis” in the following, sign – leads to a “right circular axis”. On the other hand, Eq. (5) shows that launching a right-circular polarized wave along a left-circular axis leads to the generation of

the Voigt wave with the same left circular polarization than the axe (and vice-versa), so the initial right circular polarized wave is distorted along its path.
For its usefulness in the next subsection, let us write (from the **D** transversal character) the third electric field component after a path *L* as:

$$E_3(L) = -\frac{\underline{\underline{\varepsilon}}_{31} E_1(L) + \underline{\underline{\varepsilon}}_{32} E_2(L)}{\underline{\underline{\varepsilon}}_{33}} \qquad (7)$$

2.2 The energy flow for wave propagation along an optical axis

The instantaneous energy flow at a given spatial position **r** can be obtained from the instantaneous Pyonting vector $\mathcal{P}(\mathbf{r}, t) = \mathcal{E}(\mathbf{r}, t) \times \mathcal{B}(\mathbf{r}, t) / \mu_0$ (real vectors), the latter being the real part of the complex instantaneous Poynting vector **P**(**r**, t):

$$\mathcal{P}(\mathbf{r}, t) = (\mathbf{P}(\mathbf{r}, t) + \mathbf{P}^*(\mathbf{r}, t)) / 2 \qquad (8)$$

Then introducing the complex electric and magnetic monochromatic fields **E**(**r**, t) and **B**(**r**, t), we can decompose **P**(**r**, t) in two parts:

$$\mathbf{P}(\mathbf{r}, t) = \mathbf{P_1}(\mathbf{r}, t) + \mathbf{P_2}(\mathbf{r}) \qquad (9$$

With :

$$\mathbf{P_1}(\mathbf{r}, t) = \mathbf{E}(\mathbf{r}, t) \times \mathbf{B}(\mathbf{r}, t) /(2\mu_0) \qquad (10)$$

$$\mathbf{P_2}(\mathbf{r}) = \mathbf{E}(\mathbf{r}, t) \times \mathbf{B}^*(\mathbf{r}, t) /(2\mu_0) \qquad (11)$$

The real part of $\mathbf{P_1}(\mathbf{r}, t)$ represents the time dependent energy flow while the real part of $\mathbf{P_2}(\mathbf{r}) = \langle \mathbf{P}(\mathbf{r}, t) \rangle$ is the energy flow averaged on one period of time. The magnetic field in (9) and (10) is obtained inserting the electric field of the wave from subsection 2.2 Eq. (5) inside Maxwell-Faraday equation.

As an illustration let us consider the $\begin{bmatrix} 1 \\ i \end{bmatrix}$ left-circular polarized wave propagation along the left-circular optical axis. Eq. (5) simplifies drastically. The expression of the average Poynting vector is after a path L:

$$\langle \mathbf{P}(\mathrm{L}) \rangle = \frac{k^* e^{-2k''L}}{2\omega\mu_0} \left[-\frac{E_3(0)}{2} \begin{bmatrix} 1 \\ -i \end{bmatrix} \right] \qquad (12)$$

which exhibits with an evident notation a 2-dimension transverse part and a 1-dimension longitudinal part. In Eq. (12) the wave-number has been decomposed in real and imaginary part: $k = k' + i\,k''$.
The time varying part Pyonting vector is:

$$\mathbf{P_1}(\mathrm{L}, \mathrm{t}) = -\frac{k e^{2i(kL-\omega t)}}{2\omega\mu_0} \left[\frac{E_3(0)}{0} \begin{bmatrix} 1 \\ i \end{bmatrix} \right] \qquad (13)$$

which reduces to a transverse part.

2.3 The dielectric susceptibility due to the Nd^{3+} impurities in the KGW crystal

Let us recall that the two-fold **b** crystallographic axis of the KGW crystal coincides with the **Np=X** (=**b**) principal axis of the dielectric frame. The two other **Nm=Y** and **Ng=Z** principal axes lie in the **a**-**c** crystallographic plane [2] (we use bold letters for vectors and normal letters for numerical values, for example the **Np**, **Nm**, **Ng** axes are associated respectively to the n_p, n_m, n_g refractive indices).

The permittivity tensor of the undoped and transparent crystal is real and related to the refraction indices: $\varepsilon'_{ii} = \epsilon_0 n_i^2$ (ε'_{ij} diagonal in the dielectric frame; *i, j*=**X**, **Y**, **Z**). Of course we keep in mind that the n_i refractive indices are frequency dependent trough KGW Sellmeier formula, but we do not insist to this point at this step.

Doping the crystal with Nd^{3+} impurities leads to an additional dielectric susceptibility $\varepsilon_0\chi_{ij}(\nu)$ strongly frequency-dependent near the absorption lines corresponding to transitions from the $^4I_{9/2}$ ground state towards the upper levels. The ε tensor appearing in the right side of Eq. (1) is then:

$$\varepsilon_{ij} = \varepsilon'_{ij} + \epsilon_0\chi_{ij}(\nu) \qquad (14)$$

We restrict our talk to the $^4I_{9/2} \rightarrow {}^4F_{5/2}$ transition around 800 nm and, as an illustration, we consider a lone oscillator whose absorption line is centered at ν_0 frequency. If the crystal was orthorhombic the $\chi_{ij}(\nu)$ tensor should be diagonal in the dielectric frame but the monoclinic symmetry of the KGW crystal allows a θ_0-rotation around the two-fold **b**-axis (=**X**) of the **Y'** and **Z'** oscillator axes (of course **X'=X**), so off-diagonal complex elements appear:

$$\begin{bmatrix} \chi_{XX} & 0 & 0 \\ 0 & \chi_{YY} & \chi_{YZ} \\ 0 & \chi_{YZ} & \chi_{ZZ} \end{bmatrix} = \begin{bmatrix} 1 & 0 & 0 \\ 0 & \cos\theta_0 & \sin\theta_0 \\ 0 & -\sin\theta_0 & \cos\theta_0 \end{bmatrix} X \begin{bmatrix} \chi_{X'X'} & 0 & 0 \\ 0 & \chi_{Y'Y'} & 0 \\ 0 & 0 & \chi_{Z'Z'} \end{bmatrix} X \begin{bmatrix} 1 & 0 & 0 \\ 0 & \cos\theta_0 & -\sin\theta_0 \\ 0 & \sin\theta_0 & \cos\theta_0 \end{bmatrix} \qquad (15)$$

where we have not repeated the frequency dependence. Finally, choosing to model the absorption line by a Lorentzian shape and separating the $\chi_{i'j'}(\nu)$ tensor in the right side of Eq. (15) (i', j' = **X'**, **Y'**, **Z'**) in its real and imaginary part [38], we obtain:

$$\chi_{i'i'}(\nu) = \chi'_{i'i'}(\nu) + i\chi''_{i'i'}(\nu) \qquad (16)$$

$$\chi'_{i'i'}(\nu) = \frac{2(\nu_0-\nu)}{\Delta\nu}\chi''_{i'i'}(\nu) \qquad (17)$$

$$\chi''_{i'i'}(\nu) = \frac{C\lambda^3}{8\pi^3 t_{spon}\Delta\nu n}\frac{1}{1+[4(\nu-\nu_0)^2/(\Delta\nu)^2]} \qquad (18)$$

where C is the Nd^{3+} concentration.

The maximum (or minimum) absorption outside the principal axes propagation directions involved by the rotation of the imaginary part of the tensor permittivity was already encountered in monoclinic laser materials, for example in Nd doped YCOB [41], but in the formula (15) the rotation description involves the full complex additional dielectric susceptibility. So the θ_0 rotation depends on the transition and in case of several transitions (case not explicitly written here) this angle is wavelength dependent and is a fourth spectroscopic parameter [42].

3. Experimental methods

The CW beam used for imaging was provided by a Coherent Titane-sapphire laser pumped by a frequency doubled Nd:YAG laser at 532 nm. The beam wavelength was tunable from 750 up to 900 nm with 0.01 nm spectral width.

The optical axes of the KGW biaxial crystal at a wavelength where it is transparent lie in the **Np**-**Ng** principal plane, more precisely with V_g=46.4° polar angle from the **Nm** axis at 790 nm [5]. In this study we used two 3% Nd-doped crystals from Molecular Technology GMBH oriented along an optical axis as it is shown in Fig. 1 (a) and mounted on a holder equipped with three perpendicular rotation axes (one vertical and two horizontal). The crystals were 6X6X3.15 mm^3 and 6X6X1 mm^3 in sizes. We operated the orientation of the samples with

classical conoscopy: a convergent beam obtained with 3 cm focal length doublet was sent through the front face of the crystal at a wavelength which is not absorbed by the Nd^{3+} ions: 790 nm wavelength. The output divergent beam from the exit crystal face was detected at the focal plane of a 10 cm focal length doublet by a CCD camera from Ocean Optics (each of the 1380X1024 pixels corresponds to a given propagation direction inside the crystal). The pixel size is 15 µm and the full field of view is 11.4° X 8.5°. With 15 µm pixel size, the geometric resolution is better than 10^{-2} degrees for the external angle of propagation and close to twice less for the internal angle (because the refractive indices are not far to 2).
When the input light is linear horizontally polarized and a vertical polarizer is placed in front of the camera, the obtained camera intensity shows the well-known distribution in Fig 1 (b) after adjusting the rotation axes of the crystal holder. The light extinction near the horizontal line means that the **Np**-**Nm** principal plane was horizontally oriented with the optical axis in the centre. An accurate position of the optical axis is obtained using an input left circular polarized light and an output right circular polarized analyser, adding two quarter-wave plates with their fast and slow axes at 45° from the vertical. The obtained well-known picture is constituted by concentric rings with the centre corresponding to the optical axis (Fig. 1 (c)).
The angular radius of the first dark ring was measured to be 0.225°. It corresponds to 2π dephasing of the two components of the input circularly polarized light at 790 nm after propagation through the crystal and the angular radius can be calculated from the n_p, n_m, n_g refractive indices. However, using the indices given in [5] for KGW:Nd or in [43] for undoped KGW, it was not possible to get the experimental ring value (neither the V_g value with data of [43]). We chose to recalculate the and n_p, n_m and n_g values in order to get simultaneously the V_g =46.4° polar angle of the optical axis, the first dark ring radius from conoscopy and, anticipating the study given in the next section 4.4, the semi-angle A of the hollow cone from internal conical refraction. The result is n_p=1.9809, n_m=2.0135 and n_g=2.0445.

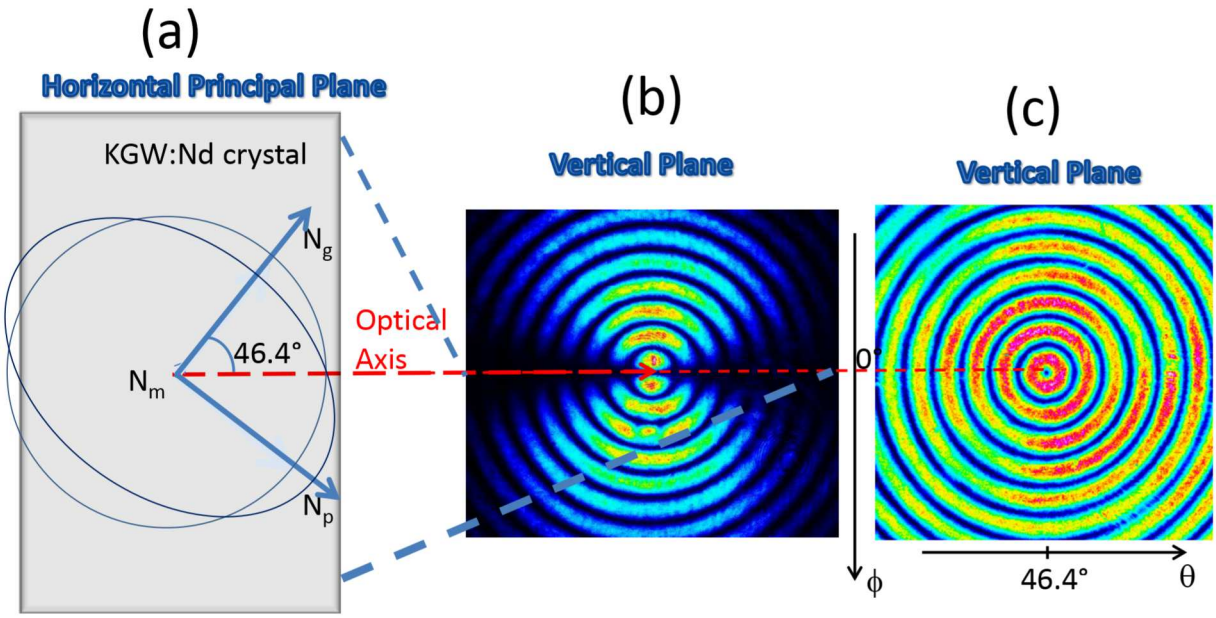

Fig. 1 (a) KGW:Nd crystal and its orientation, (b) conoscopy figure obtained with two vertical and horizontal crossed linear polarizers, (c) conoscopy figure obtained with two left and right crossed circular polarizers.

For conical refraction imaging, the input laser beam was focused on the entrance face of the KGW:Nd crystal with the 3 cm focal length doublet. The image of the different planes inside

or outside the crystal was obtained with a 5 cm focal length doublet on the CCD camera located at 2.86 m. The image magnification was close to 56. Circular or linear polarizers can be placed on the input and the output beams.

4. Voigt wave investigation

4.1 Anisotropy of the absorption

The absorption lines of the Nd doped KGW crystal are strongly anisotropic. We have represented in Fig. 2 (a) the ones corresponding to the $^4I_{9/2} \rightarrow {}^4F_{5/2}$ transition in **Nm** and **Ng** polarizations from a home-grown additional sample elaborated as a platelet with large transparent faces perpendicular to the b-axis. The main peak is at 810.6 nm. We have modeled (dashed line in Fig. 2 (a)) the **Nm**-polarized main absorption line with 1.8 nm full width at half maximum from formula (18) giving the imaginary part $\chi''_{Y'Y'}(\lambda)$. From formula (17) we have represented the real part $\chi'_{Y'Y'}(\lambda)$ by the blue line in Fig. 2 (a). For a better visualization an adapted arbitrary figure scale has been used (let us recall that we have the connection $\chi'' = \frac{\lambda n}{2\pi}\Gamma$ where Γ is the peak absorption coefficient). Let us point out the well-known feature [32] useful in the following section 4.3: the $\chi'_{Y'Y'}(\lambda)$ extrema occur at half-peak absorption value; outside the range of wavelengths between the two extrema the additional refractive index carried by the Nd impurities is positive (large wavelengths) or negative (low wavelengths) and no change occurs at the peak wavelength.

We have modeled the $\chi_{i'i'}(\lambda)$ tensor of the optical axis–oriented sample corresponding to the **Np** and **Ng** polarizations in such a way that the three polarized 810.6 nm peak absorptions are in the ratios measured in [3]: σ_p=7.81 10^{-20} cm^2, σ_m=26.75 10^{-20} cm^2, σ_g=3.43 10^{-20} cm^2. We have adjusted 1.8 nm as full width at half maximum of the Lorentzian line and 60 cm^{-1} as peak absorption in **Nm** polarization in order to describe at best the experimental results in the next 4.2 and 4.3 sections.

Of course it is clear from Fig. 2 (a) that several oscillators should be necessary for a full description of the absorption properties.

The angular distribution of the optical axis-oriented sample transmission was recorded with the CCD camera and the conoscopy set-up of section 3 at 810.6 nm wavelength. The center of a cross on the camera screen is used to mark out the optical axis of the crystal at a wavelength where it is transparent (790 nm). The horizontal line of the cross represents propagation directions in the **Np**-**Ng** principal plane (see Fig. 1). In a first step the input light was linearly polarized and the polarizer was -10° and 80° rotated to find respectively the minimum and the maximum of the transmission at the center of the cross. Inserting a linear analyser between the crystal and the camera, we checked that these transmission extrema correspond to output light with the same linear polarization than the input. These extrema are quite different in transmission intensity and because along its propagation path a two-component wave polarization will rotate towards the less absorbed component, it is clear that the propagation direction corresponding to the center of the cross is no more an optical axis at the absorbed wavelengths (the new optical axes positions outside the $\varphi = 0$ principal plane are studied in the two following sub-sections). The output light distribution for the minimum transmission at the cross center is visualized in Fig. 2 (b) after zooming the camera screen (the field of view is 2.85° X 2.1°) and exhibits a narrow dark domain going through the cross center. This narrow angular domain is inclined with respect of the **Np**-**Ng** principal plane trace with an angle about 15°. The interpretation of the transmission rotation is formula (15). The two experimental values of the deviation from vertical (80° and -10°) of the two mode polarizations at the center of the cross can be calculated nicely with expression (7) of ref. [38] (they are very close to be linear) using θ_0 = 12° rotation in Eq. (15).

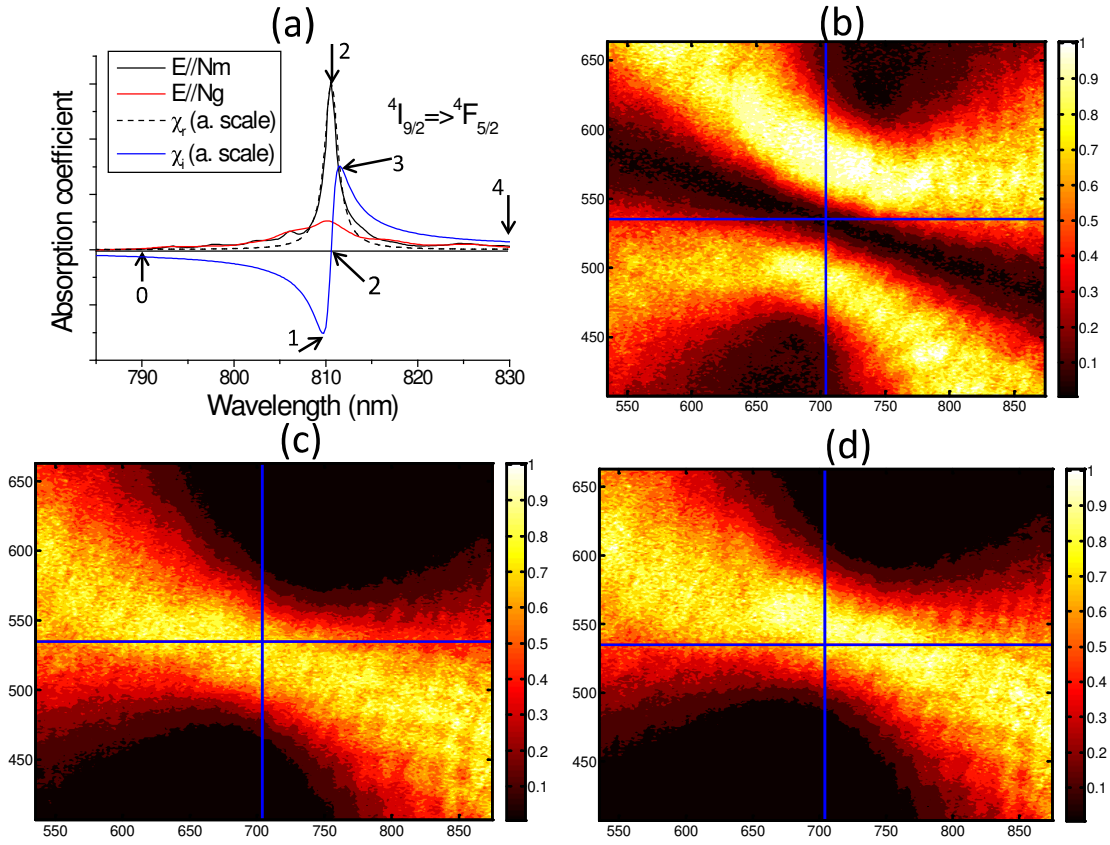

Fig. 2: (a) Example of $^4I_{9/2} \rightarrow {}^4F_{5/2}$ absorption spectra of KGW:Nd in two polarizations near 810 nm and the main line modeled in arbitrary scale; (b), (c), (d): transmission angular distribution in arbitrary units at 810.6 nm of the optical axis-oriented KGW:Nd sample respectively in linear, right-circular and left-circular input polarizations. The cross center is the location of the optical axis of the transparent crystal (790 nm).

As it is pointed out in literature [37] for absorbing crystals, the modes along propagation directions in the vicinity of the optical axes are elliptically polarized or even circularly polarized on the axes (useful formulas are also written in [38]). Their full experimental evidence pixel by pixel should be time consuming so we simplified it launching a left or right circular polarized laser light at 810.6 nm and recording its transmission with the camera. The result is seen in Fig. 2 (c) (right-circular polarization) and 2 (d) (left-circular polarization). The angular domain corresponding to the highest transmission is displaced below the cross center in the right-circular case (Fig. 2 (c)) and above in the left-circular case (Fig. 2 (d)). This feature can be calculated with formulas (3) and is in agreement with the following section 4.2 devoted to the Voigt wave.

4.2 Voigt wave investigation

The investigation was based on the conoscopy set-up described in section 3, the *L*=3 mm thickness Nd :KGW sample being placed between two crossed left (L) and right (R) circular polarizers. Starting at the 790 nm non-absorbed wavelength, the optical axis of the crystal appears extinguished (in dark) in the centre of the rings as in Fig. 1 (c). Then the wavelength was progressively moved in the absorption spectra of Fig. 2 (a) towards absorbed wavelengths. Of course the general intensity of the camera image decreased drastically but its luminosity and contrast can be satisfyingly restored playing with the exposure time. At moderate absorption we observed that the optical axis deviates progressively from the center of the rings and moved towards and inside the first brilliant ring. An example of this behaviour is provided at 808.8 nm in Fig. 3 (a), the input light being right-circular polarized

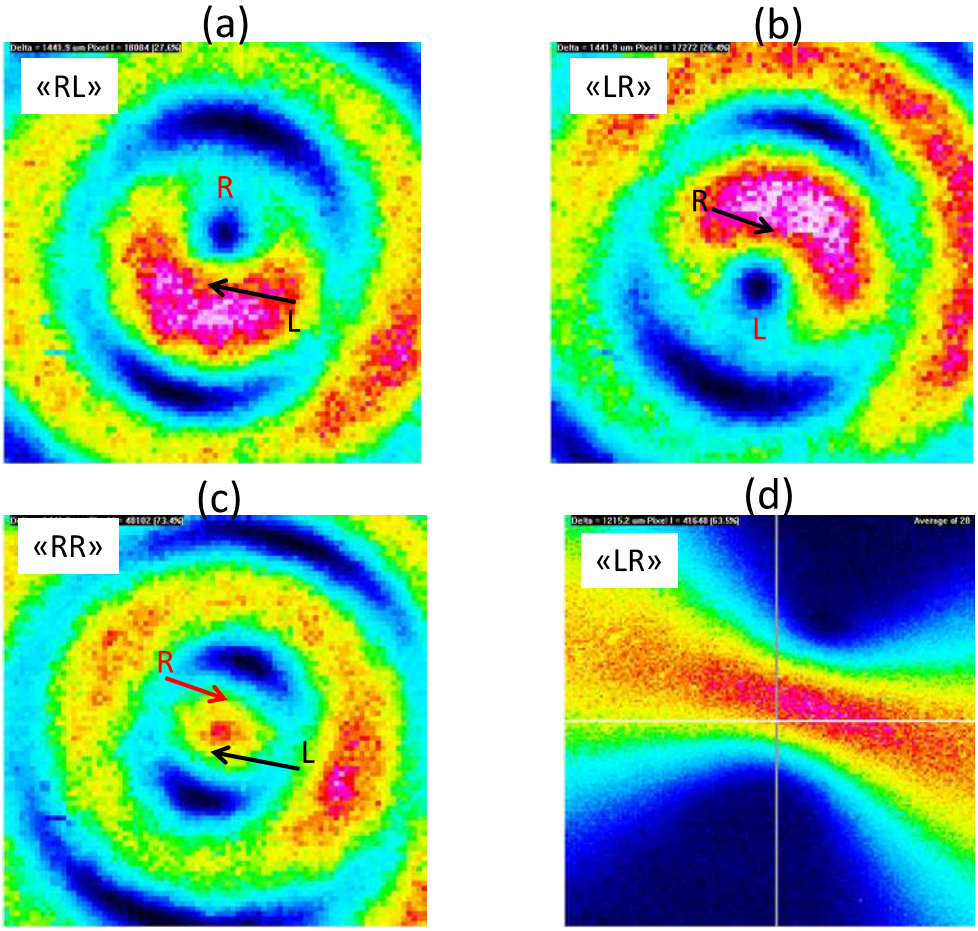

Fig. 3: (a), (b), (c) Conoscopy picture at 808.8 nm in "RL", "LR" and "RR" configurations (see text) respectively; (d) conoscopy picture at 810.6 nm in "LR" configuration.

and the output analyser being left-circular polarized ("RL" configuration). If the circular polarizers and analysers are reversed ("LR" configuration), the optical axis displacement (Fig. 3 (b)) is distinct than in the previous case (apparently it is an opposite direction). When the wavelength approaches the 810.6 nm peak absorption the optical axis displacement continued but the rings are strongly deformed and even can be hardly recognized (Fig. 3 (d)). The complete study of the optical axis displacement versus wavelength is provided in the following section 4.3. From now in the present section we fix the wavelength at 808.8 nm where the **Nm** absorption coefficient is 12 cm^{-1}.

So the optical axis of the transparent crystal was split by absorption in two new optical axes in agreement with literature [35] and with the theoretical discussion in section 2.1 (Eq. (4)). The optical axis evidenced by the "LR" configuration propagates unchanged a left-circular polarized light and can be labelled "L" (the dark point in Fig 3 (b)), the wave propagation being described setting $\begin{bmatrix} E_1(0) \\ E_2(0) \end{bmatrix} = \begin{bmatrix} 1 \\ i \end{bmatrix}$ in Eq. (5) used with sign +. The other axis can be labelled "R" (dark point in Fig. 3 (a)). At this step the key-point is to mark out the "L" axis in Fig. 3 (a) and the "R" axis in Fig. 3 (b), they are situated in a brilliant domain and reveal the Voigt wave as we can explain easily. For example, launching the R-circular $\begin{bmatrix} 1 \\ -i \end{bmatrix}$ wave along the "L" axis is described with Eq. (5) sign + and the output from the crystal is: $\left\{ \begin{bmatrix} 1 \\ -i \end{bmatrix} + ikL \frac{\delta_{12}}{\delta_{11}+\delta_{22}} \begin{vmatrix} 1 & 1 \\ i & -i \end{vmatrix} \begin{bmatrix} 1 \\ i \end{bmatrix} \right\} e^{ikL}$. The second term (Voigt wave) is L-circular polarized and is

transmitted by the output L-circular analyser, so the output intensity has a significant intensity in the "RL" picture 3 (a).
Two other configurations are of interest: the "RR" and the "LL". They are very similar, one of them is shown in Fig. 3 (c), on which it is also useful to mark out the two "L" and "R" optical axes.

We have measured the light intensity transmitted through the L=3 mm thickness sample for the propagations along the two "L" and "R" optical axis in the various "LR", "LL", "RL" and "RR" configurations. Then we have extracted the physical parameters of interest according to the theoretical description of the wave propagation. Launching a R-circular or a L-circular wave of unity intensity along a "L" or a "R" optical axis respectively, the transmitted time average intensity I obtained from the usual scalar product with the trans-conjugate wave-vector [40] is simply:

$$I = e^{-\gamma L} + c_V L^2 e^{-\gamma L} \qquad (19)$$

$$c_V = 4|k|^2 \left|\frac{\delta_{12}}{\delta_{11}+\delta_{22}}\right|^2 \qquad (20)$$

γ=2k" is the absorption coefficient, c_V is a coefficient characterizing the Voigt wave intensity. So the intensity is the sum of the intensities of the component which is propagated unchanged and of the Voigt component. The angular position of the optical axes is calculated solving Eq. (4) numerically. The results (γ and c_V) are gathered in Table 1 with some obvious notations. The various configurations are understood keeping in mind that the first term circular polarization in formula (19) is given by the circular input polarizer and that the second term

Table 1 Physical parameters obtained from conoscopy in various configurations at 808.8 nm.

				Output wave	
	Polarizer	crystal output	Analyser	theoretical	experimental
"L" optical axis	L	L	R	0	
	L	L	L	exp(-γL); γ=7.3 cm^{-1}	γ=10.1 cm^{-1}
	R	R + L_Voigt	R	exp(-γL); γ=7.3 cm^{-1}	γ=9.6 cm^{-1}
	R	R + L_Voigt	L	L_Voigt ; c_V=25.7 cm^{-2}	c_V=20.1 cm^{-2}
"R" optical axis	R	R	L	0	
	R	R	R	exp(-γL); γ=7.3 cm^{-1}	γ=10.7 cm^{-1}
	L	L + R_Voigt	L	exp(-γL); γ=7.3 cm^{-1}	γ=10.1 cm^{-1}
	L	L + R_Voigt	R	R_Voigt; c_V=25.7 cm^{-2}	c_V=18.7 cm^{-2}

(Voigt component) has the circular polarization characterizing the optical axis along which the wave propagates. The experimental and calculated γ and c_V values in Table 1 are in reasonable agreement, taking into account the debasement of the CCD images due to the residual speckles, which are the main limitation to the accuracy of the measured light intensity.
In another set of investigations, we compared the transmitted intensities launching circularly polarized waves along a given optical axis simply by removing the circular analyser. The result is that if the input light is of opposite circular polarization than the optical axis, for example a R-polarized light launched along a "L" axis, the transmitted intensity is much

higher than if both the input light and the optical axis have the same circular polarization. This is clearly seen reading the lines with "removed" analyser in Table 2. More, the transmitted intensity red in the "Full wave" lines in Table 2 is close (within10%) to the sum of the intensities of the two following lines of the Table in agreement with formula (19) and its two-component decomposition. In laser applications with propagation along an optical axis [19, 20], in principle, the pumping stage will be affected by the fact that the absorption is less efficient if the input light is of opposite circular polarization than the optical axis, which is another expression of the anisotropy of the absorption expressed by the Voigt wave . Despite of the fact that generally the pump is non-polarized and that it is divergent enough to propagate simultaneously along the two optical singular axes, a full understanding of the laser efficiency should require the measurement of the absorbed pump power, to be compared with the theoretical prediction. In the following 4.4 subsection another aspect of absorption anisotropy is provided. More, the lasing wave property could be influenced by the voigt component inside the anisotropic gain medium. This aspect is currently studied by the author and is outside the scope of the present paper.

We compared finally the forward and backward propagations along an optical axis at the fixed 808.6 nm absorbed wavelength. Marking carefully on the camera screen the "L" axis (forward propagation) with the "LR" configuration of the circular polarizers (it is a dark spot), we 180° rotated the KGW crystal around the vertical **Nm** axis. Doing so, the backward propagation corresponding to the initial optical axis forward propagation was easily located on the camera screen. Playing with the two circular polarizers configurations we determined that the light extinction was obtained in "RL" configuration, meaning that the backward propagation occurs along a "R" axis. Of course we verified the same axis inversion starting with the initial "R" axis forward propagation.

These observations are supported by the theory developed in section 2.1. Starting with a (θ, ϕ) forward direction of propagation, the backward propagation can be described by the $(\pi-\theta, \phi+\pi)$ propagation. In such transformation the δ_{11} and δ_{22} coefficients are unchanged but the δ_{12} coefficient changes its sign, so in Eq. (4) the $\pm$ in changed into $\mp$, meaning that if the initial forward (θ, ϕ)-propagation was along a "L" axis, then the backward $(\pi-\theta, \phi+\pi)$-propagation will be along a "R" axis and vice-versa. In other words, Eq. (4) has four (θ, ϕ) solutions leading to four "L" optical axes and four (θ, ϕ) solutions leading to four "R" optical axes, these solutions being grouped by pairs of forward and backward propagations.

4.3 Optical axes directions versus the absorption wavelength

Starting at the 790 nm non-absorbed wavelength, the optical axis of the transparent crystal appears extinguished in the centre of the rings in Fig. 1 (c) and in Fig. 4. As we said previously in section 4.2 from the two "LR" and "RL" configurations, when the laser wavelength was progressively increased (by 0.3 nm steps or half this value, with 0.01 nm bandwidth) in the absorption spectra of Fig. 2 (a) towards increasing absorption (direction of the markers labelled 0, 1, 2, 3, 4 corresponding respectively to the wavelengths 790, 809.7, 810.6, 811.6, 830 nm), the optical axis splits and gives rise to two new ones labelled "L" and "R". These new axes separate and their angular orientation versus wavelength has been reported as blue squares ("R" axis) and red circles ("L" axis) in Fig. 4 (in this picture the rings obtained from the transparent crystal at 790 nm are in background and help visualizing as a cartography). The optical axes displacement, following the markers 0, 1, 2, 3, 4, is complex and reveals four optical phenomena:

- due to the anisotropy of the absorption, the optical axis of the transparent crystal (marker 0) cannot remain an optical axis at absorbed light wavelengths, the optical

axis splits in two new “L” and “R” ones and the imaginary part of the dielectric susceptibility tensor (formula (14)) explains quite well this behaviour

- for the range of wavelengths between the markers 0 and 1, the real part (Fig. 2 (a)) of the additional Nd tensor (formula (18)) is negative and its trend is to decrease the refractive index in **Nm** polarization. This occurs also for the **Np** and **Ng** polarizations but in a much weaker proportion due to the preponderance of the **Nm** absorption line. The net effect is a relative decrease of the ordinary refractive index (**Nm** polarization) in Fig. 1 (a), leading the optical axis to approach the **Ng** direction and moving towards the left part of the camera screen (Fig. 1 (c) and Fig. 4). In the range of wavelengths between the markers 1 and 3, the real part of the additional Nd tensor increases and the optical axis tends towards the right part of the camera screen. At the maximum absorption wavelength (marker 2) the real part of the additional Nd tensor is zero and the separation between the two “L” and “R” optical axes is maximum (the imaginary part is maximum).
- a general rotation, let us say about 15°, can be guessed by inspection of the two loops described by the blue squares and the red circles in Fig. 4. This can be described by the rotation of the full complex additional Nd dielectric susceptibility in formula (15).
- for the range of wavelengths between the markers 3 and 4, the additional Nd refractive index decreases and tends towards its initial value. However, we can see in Fig. that the marker 4 does not coincide with the initial marker 0. Going to wavelengths much shorter than 790 nm confirms that the optical axis of the transparent crystal is located below marker 0 and above marker 4 for wavelengths much larger than 830 nm. This effect could be explained by a slight rotation around the two-fold b-axis of the dielectric frame of the undoped KGW (allowed by the monoclinic symmetry and measured in some crystals as BiB_3O_6 for example) and it is not at the heart of the present study. Nevertheless an attempt was done to get a quantitative description introducing 0.04°/40 nm rotation of the dielectric frame.

Table 2 Transmitted light obtained from conoscopy in various configurations at 808.8 nm.

				Output wave	
	Polarizer	crystal output	Analyser	theoretical	Experimental (a. u.)
"L" optical axis	R	R + L_Voigt	Removed	Full wave	6667
	L	L	Removed	exp(-γL)	2428
	R	R + L_Voigt	L	L_Voigt	4631
	R	R + L_Voigt	R	exp(-γL)	2654
"R" optical axis	L	L + R_Voigt	Removed	Full wave	6306
	R	R	Removed	exp(-γL)	3656
	L	L + R_Voigt	R	R_Voigt	4455
	L	L + R_Voigt	L	exp(-γL)	2509

We have performed the quantitative description of the “L” and “R” optical axes displacement versus wavelengths solving numerically Eq. (4), using the refractive indices at 790 nm given in section 3, the peak absorption coefficients at 810.6 nm and the line width given in section 4.1 and 12° as the θ_0 rotation in formula (15). The results are represented by the blue and red dashed lines in Fig. 4. The general behaviour of the

displacement is predicted satisfactorily. Including more absorption lines should be of course necessary to get the full agreement with the experimental data.

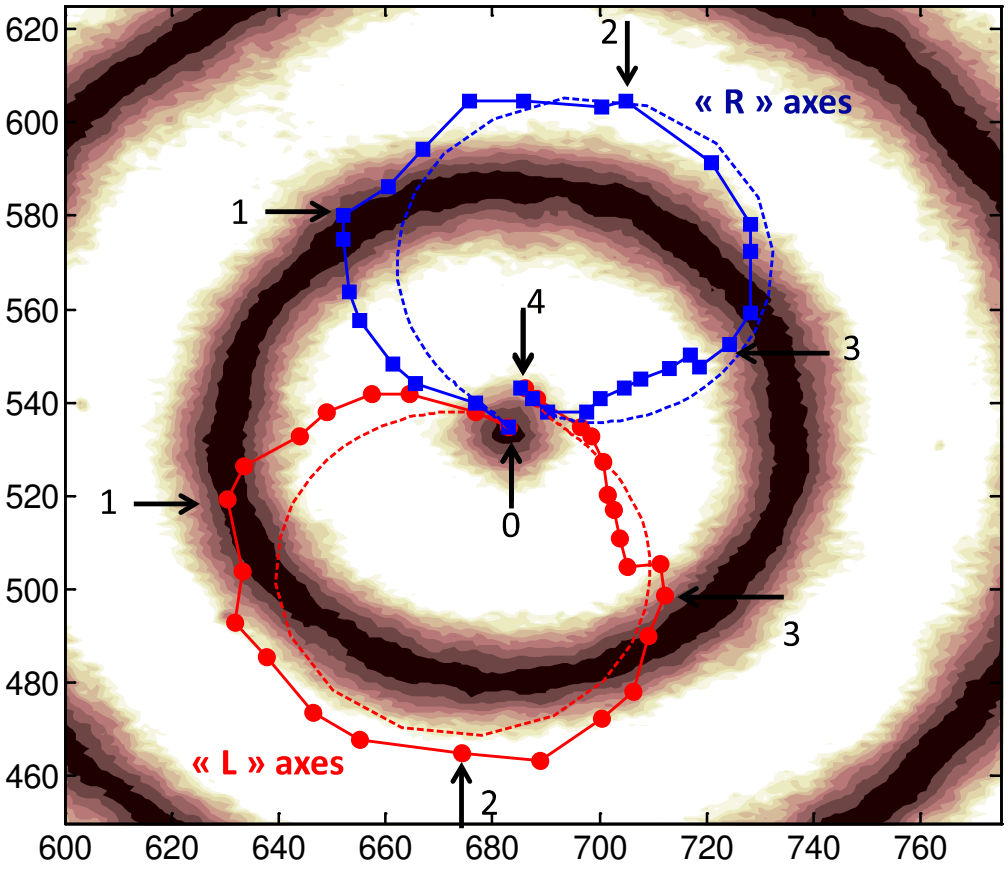

Fig. 4: Directions of the two "L" and "R" optical axes versus the wavelengths of the $^4I_{9/2} \rightarrow {}^4F_{5/2}$ absorption spectra. The arrows report on wavelengths marked out in Fig. 2 (a). The squares and circles are experimental, the dashed lines are theoretical.

4.4 Conical refraction at absorbed wavelengths

In a first step we worked at 790 nm, which is a wavelength of transparency for the KGW:Nd crystal, with a circularly polarized input light. The position of the output lens was tuned in order to get the image of the beam focus (near the entrance face of the crystal) on the camera screen. For propagation directions which deviate significantly of the optical axis, the usual double refraction was observed, i. e. two distinct small brilliant areas. Attempts, with the help of the two orthogonal rotation axes of the crystal holder, to make the collapse of these two areas lead in fact the light to condense inside a sharp ring (Fig. 5 (a)) with inside a narrow dark one. This is the internal conical refraction effect that we have presented in the introduction, corresponding mainly to plane waves propagating in the direction along an optical axis. However the input beam (section 3) is a focused Gaussian one and under these circumstances the energy directions delimit the dark ring [18]. More, several authors in the past have shown that it was possible to exhibit two "Raman spikes" moving away the imaging lens in two opposite directions, corresponding to the external conical refraction (Fig. 5 (c)). Between these two positions we can find a plane inside which the light is distributed in the "Poggendorff rings" (Fig. 5 (b)).

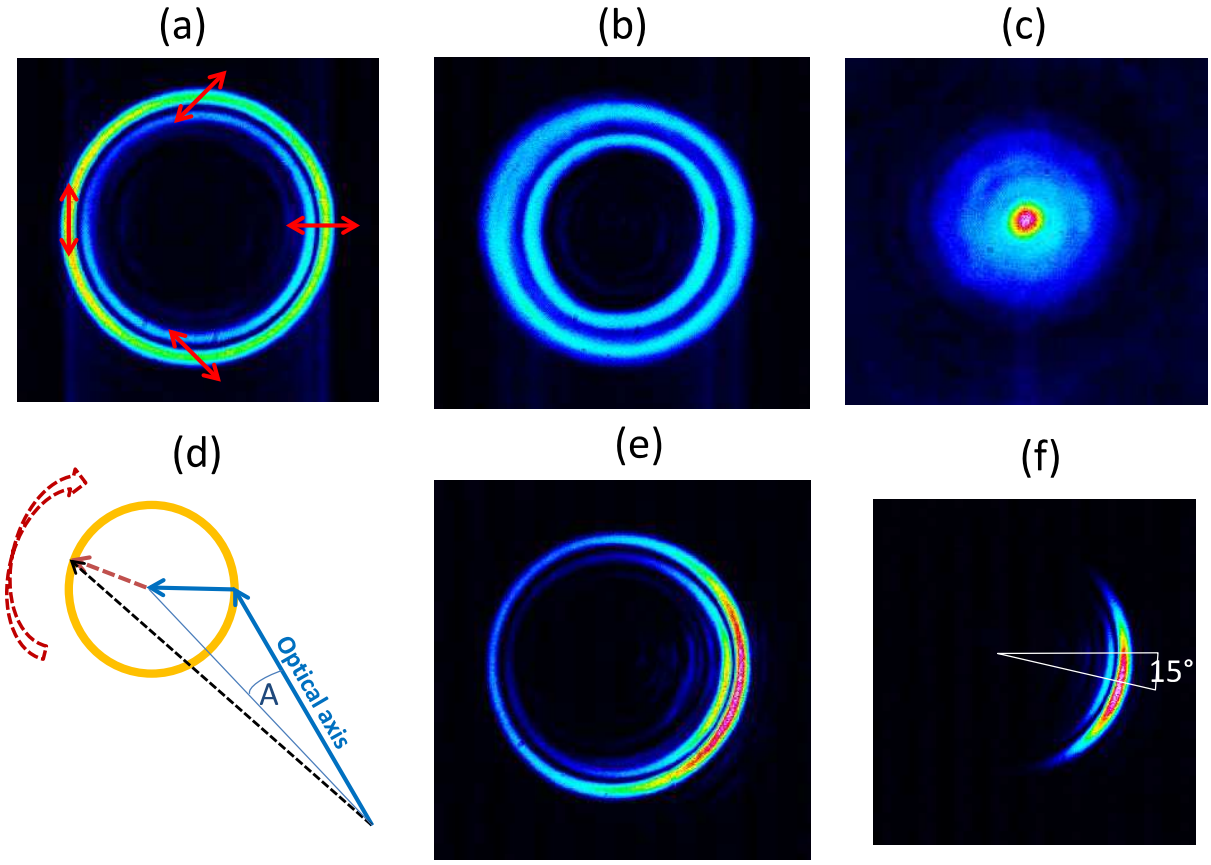

Fig. 5 (a), (b), (c) Conical refraction images at 790 nm wavelength corresponding to the focal plane, the Poggendorff rings and the Raman spikes respectively; (e), (f) images of the focal plane at 808.8 and 810.6 nm respectively.

The radius of the internal conical refraction dark ring was easily measured on the camera screen (5572 µm), then the semi-angle A of the hollow cone is deduced to be 0.0158 rad. This value was calculated by anticipation in section 3 with the expression:

$$tg(A) = \frac{1}{2}\frac{\sqrt{(n_m^2 - n_p^2)(n_g^2 - n_m^2)}}{n_p n_g} \qquad (21)$$

which originates from the ratio of the transverse and longitudinal average Pyonting vector components (real parts) in formula (12). In Fig. 5 (d) we have represented these two time-independent components with the blue solid arrows (the longitudinal component is parallel to the optical axis); due to our set-up visualized in Fig. 1 (a) they are located in the horizontal **Np**-**Ng** principal plane. The full Poynting vector (black dashed arrow in Fig. 5 (d)) is obtained adding the time varying transverse part (formula (13) represented by the red dashed arrow in Fig. 5 (d)). The end of the latter vector describes the brilliant circle at twice the rotation rate of the electric field. The energy propagation along the optical axis corresponds to an ordinary wave and the polarization of the electric field is vertical. Let us notice that the optical axis is represented towards the right part of the circle in Fig 5 (d) while the associated vertical electric field is represented by the red arrow in the left part of the circle in Fig. 5 (a) (this position was experimentally verified with a linear vertical polarizer). The reason of this inversion is of course the imaging lens. Similarly a horizontal linear polarizer allows checking the horizontal polarization of the wave at the right part of the circle in Fig. 5 (a) (propagation of the extraordinary wave in the **Np**-**Ng** principal plane, towards the left of the circle in Fig 5 (d) in agreement with the surface indices orientation in Fig. 1 (a)). The other polarizations along the brilliant circle are checked to be in intermediate orientations.

The last step was to shift the input laser beam wavelength towards the absorption peak. We show in Fig. 5 (e) how the light intensity starts to decrease in the left side of the circle at the 808.8 nm intermediate wavelength. At the peak absorption (810.6 nm) the light is transmitted only in a crescent-shaped area on the circle (Fig. 5 (f)). The diameter linking the most and the less intense light is 15° inclined from the horizontal **Np**-**Ng** principal plane. This is the same inclination than the central narrow dark area in Fig. 2 (b), meaning that the common origin of the light absorption in the two experiments is the anisotropy of the absorption. In other words the transmitted light corresponds to the less absorbed linear component of the polarization and the light distribution is similar to the one obtained with a non-absorbed wavelength (790 nm) through an output linear polarizer conveniently rotated. In laser applications, care must be taken for the pump beam to fill the whole volume enclosed by the refraction cone [20] of the laser wave. A refined analysis could take into account the crescent shape of the absorbed beam.

5. Conclusion

We have investigated the Nd^{3+}-doped KGW biaxial laser crystal for wave propagation directions in the vicinity of the optical axis at wavelengths tunable in the absorption domain around 800 nm, corresponding to the $^4I_{9/2} \rightarrow {}^4F_{5/2}$ transition usually involved in laser diode pumping. The spectral resolution (0.01 nm) of the employed laser beam was much better than the absorption linewidths (1.8 nm) and the angular resolution of the set-up was as high as 10^{-2} degrees. The angular distribution of the absorption was found strongly anisotropic and highly polarization-dependent, especially at the 810.6 nm peak. The properties of the optical axes have been investigated versus the light absorption. Starting at a wavelength where the crystal is transparent (790 nm) and going towards the absorbed wavelengths, we showed how the optical axis splits in two new ones able to propagate unchanged a left or right circularly polarized light (labelled “L” and “R” respectively). Launching a left circularly polarized light along the “R” axis leads to the right circularly polarized Voigt wave propagation (and vice-versa) in addition to the isotropic propagation. The intensities of the transmitted light in different configurations of the circular polarizers have been found in agreement with the electromagnetic theory. The angular displacement of the two optical axes versus the absorbed wavelengths was measured to be complex but it could be explained reasonably well with a single oscillator model representing the Nd^{3+} ions absorption and taking into account both the real and the imaginary part of the additional dopant polarization. The light energy propagation of the waves propagating along or close to the optical axes was found distributed inside a crescent-shaped area at absorbed wavelengths in agreement with the polarization dependence of the absorption which modifies the conical refraction phenomenon.

Acknowledgments

Y. Guillin, S. Le Bec, J.-F. Sivignon and J.-M Ingargiola are greatly acknowledged for technical assistance.

References

1 C. Pujol, M. Aguilo, F. Diaz, C. Zaldo, "Growth and characterisation of monoclinic $KGd_{1-x}RE_x(WO_4)_2$ single crystals", Opt. Mater. **13**, 33-40 (1999).

2 I. V. Mochalov, "Laser and nonlinear properties of the potassium gadolinium tungstate laser crystal $KGd(WO_4)_2:Nd^{3+}$ (KGW:Nd)", Opt. Eng. **36**, 1660-1669 (1997).

3 Y. Chen, Y. Lin, X. Gong, Q. Tan, J. Zhuang, Z. Luo, Y. Huang, "Polarized spectroscopic properties of Nd^{3+}-doped $KGd(WO_4)_2$ single crystal", J. Lumin. **126**, 653-660 (2007).

4 J. M. Esmeria, Jr., H. Ishii, M. Sato, H. Ito, "Efficient continuous-wave lasing operation of Nd: $KGd(WO_4)_2$ at 1.067 μm with diode and Ti:sapphire laser pumping", Opt. Lett. **20**, 1538-1540 (1995).

5 N. S. Ustimenko and A. V. Gulin, "New self-frequency converted $Nd^{3+}:KGd(WO_4)_2$ Raman lasers", Quant. Electr. **32**, 229-231 (2002).

6 A. Brenier, "A new evaluation of Yb^{3+}-doped crystals for laser applications", Journal of Luminescence **92**, 199-204 (2001).

7 P. Wasylczyk and C. Radzewicz, "Design and Alignment Criteria for a Simple, Robust, Diode-Pumped Femtosecond Yb:KYW Oscillator", Laser Phys. **19**, 129-133 (2009).

8 S. M. Kobtsev, S. V. Kukarin and S. V. Smirnov, "Fiber Supercontinuum Generator with Wavelength-Tunable Pumping", Laser Phys. **18**, 1257-1259 (2008).

9 A. Steinmann, G. Palmer, M. Emons, M. Siegel and U. Morgner, "Generation of 9-μJ 420-fs Pulses by Fiber-Based Amplification of a Cavity-Dumped Yb:KYW Laser Oscillator ", Laser Phys. **18**, 527-529 (2008).

10 A. Major, R. Cisek, D. Sandkuijl and V. Barzda, "Femtosecond $Yb:KGd(WO_4)_2$ laser with > 100 nJ of pulse energy ", Laser Phys. Lett. **6**, 272-274 (2009).

11 Y.F. Lü, X.H. Zhang, J. Xia, R. Chen, G.Y. Jin, J.G. Wang, C.L. Li and Z.Y. Ma, "981 nm Yb:KYW laser intracavity pumped at 912 nm and frequency-doubling for an emission at 490.5 nm", Laser Phys. Lett. **7**, 343-346 (2010).

12 A. Major, D. Sandkuijl and V. Barzda, "A diode-pumped continuous-wave Yb:KGW laser with N_g-axis polarized output", Laser Phys. Lett. **6**, 779-781 (2009).

13 K. Seger, B. Jacobsson, V. Pasiskevicius, F. Laurell, "Tunable Yb:KYW laser using a transversely chirped volume Bragg grating", Opt. Express **17**, 2341 (2009).

14 A. Brenier, "Active Q-switching of the diode-pumped two-frequency $Yb^{3+}:KGd(WO_4)_2$ laser", IEEE J. Quant. Electr. **47**, 279-284 (2011).

15 A. Brenier, "Tunable THz frequency difference from a diode-pumped dual-wavelength $Yb^{3+}:KGd(WO_4)_2$ laser with chirped volume Bragg gratings", Las. Phys. Lett. **8**, 520-254 (2011).

16 S. Biswal, S. P. O'Connor, S. R. Bowman, "Thermo-optical parameters measured in ytterbium-doped potassium gadolinium tungstate", Appl. Opt. **44**, 3093-3097 (2005).

17 J. Hellstrom, S. Bjurshagen, V. Pasiskevicius, "Laser performance and thermal lensing in high-power diode-pumped Yb:KGW with athermal directions", Appl. Phys. B **83**, 55-59 (2006).

18 M. Born, E. Wolf, A. B. Bhatia, *Principles of optics: electromagnetic theory of propagation, interference and diffraction of light*, 7th ed. Cambridge University Press, 1999.

19 A. Abdolvand, K. G. Wilcox, T. K. Kalkandjiev, E. U. Rafeilov, "Conical refraction $Nd:KGd(WO_4)_2$ laser", Opt. Exp. **18**, 2753-2759 (2010).

20 J. Hellstrom, H. Henricsson, V. Pasiskevicius, U. Bunting, D. Haussmann, "Polarization-tunable Yb:KGW laser based on internal conical refraction", Opt. Lett. **32**, 2783-2785 (2007).

21 A. Turpin, Y. Loiko, T. Kalkandjiev, J. Mompart, "Free-space optical polarization demultiplexing and multiplexing by means of conical refraction", Opt. Lett. **37**, 4197-4199 (2012).
22 D. P. O'Dwyer, K. E. Ballantine, C. F. Phelan, J. G. Lunney, J. F. Donegan, "Optical trapping using cascade conical refraction of light", Opt. Exp. **20**, 21119-21121 (2012).
23 M. V. Berry, M. R. Jeffrey and J. G. Lunney, "Conical diffraction: observation and theory", Proc. R. Soc. A, **462**, 1629-1642 (2006).
24 C. F. Phelan, D. P. O'Dwyer, Y. P. Rakovich, J. F. Donegan, J. G. Lunney, "Conical diffraction and Bessel beam formation with a high optical quality biaxial crystal", Opt. Exp. **17**, 12891-12899 (2009).
25 A. Turpin, Yu. V. Loiko, T. K. Kalkandjiev, H. Tomizawa and J. Mompart, "Wave-vector and polarization dependence of conical refraction", Opt. Exp. 21 n°4, 4503-4511 (2013).
26 A. Turpin, Yu. V. Loiko, T. K. Kalkandjiev and J. Mompart, "Multiple rings formation in cascaded conical refraction", Opt. Lett. 38 n°9, 1455-1457 (2013).
27 S. D. Grant and A. Abdolvand, "Evolution of conically diffracted Gaussian beams in free space", Opt. Exp. **22**, 3880-3886 (2014).
28 V. Peet, "Experimental study of internal conical refraction in a biaxial crystal with Laguerre-Gauss light beams", J. Opt. **16**, 075702 (2014).
29 S. Rosen, G. Y. Sirat, H. Ilan, and A. J. Agranat, "A sub wavelength localisation scheme in optical imaging using conical refraction", Opt. Exp. 21, 10133-10138 (2013).
30 Z. Fang, K. Xia, Y. Yao and J. Li, "Radially polarized LG_{01}-mode Nd:YAG laser with annular pumping", Appl. Phys. B **117** n°1, 219-224, (2014).
31 Z. Fang, K. Xia, Y. Yao and J. Li, "Radially polarized and passively Q-switched Nd:YAG laser under annular-shaped pumping", IEEE J. Sel. Top. Quant. Elect. 21 (1) 1600406, (2015).
32 T. Züchner, A. Virgilio Failla and A. J. Meixner, "Light microscopy with doughnut modes: a concept to detect, characterize, and manipulate individual nanoobjects", Angew. Chem. Int. Ed. **50**, 5274-5293, (2011).
33 M. Ehrenberg, "Scientific background on the Nobel Prize in Chemistry 2014. Super-resolved fluorescence microscopy", http://www.nobelprize.org/nobel_prizes/chemistry/laureates/2014/advanced-chemistryprize2014.pdf
34 J. Q. Yao and T. S. Fahlen, "Calculation of optimum phase match parameters for the biaxial crystal $KTiOPO_4$" J. Appl. Phys. **55**, 65-68 (1984).
35 Voigt W, "On the behaviour of pleochroitic crystals along directions in the neighbourhood of an optic axis", Phil. Mag. S. 6, **4**, 90-97 (1902).
36 S. Pancharatnam, "On the pleochroism of amethyst quartz and its absorption spectra", Proc. Ind. Acad. Sci. A, **40 A**, 196-210 (1954).
37 S. Pancharatnam, "The propagation of light in absorbing biaxial crystals", Proc. Ind. Acad. Sci. **42 A**, 235-248 (1955).
38 A. Brenier, "Polarization properties of lasing near an optical axis in the biaxial $KGd(WO_4)_2$:Nd crystal", Las. Phys. Lett. **11**, 115819-115826 (2014).
39 J. Gerardin, A. Lakhtakia, "Conditions for Voigt wave propagation in linear, homogenous, dielectric medium"s, Optik **112**, 493-495 (2001).
40 Yariv A 1991 *Optical Electronics* 4th edn (USA: Saunders College Publishing)
41 Y. Petit , B. Boulanger , P. Segond, C. Félix, B. Ménaert , J. Zaccaro , G. Aka, "Absorption and fluorescence anisotropies of monoclinic crystals : the case of Nd :YCOB", Opt. Exp. **16**, 7997-8002 (2008).